J Mater Sci (2010) 45:5831–5843
DOI 10.1007/s10853-010-4659-1

Deformation mechanisms and the yield surface of low-density, closed-cell polymer foams

N. J. Mills

Received: 26 March 2010 / Accepted: 25 May 2010 / Published online: 11 June 2010

Abstract The geometry of low-density, closed-cell, polyethylene and polystyrene foams was modelled with a Kelvin foam having uniform-thickness cell faces; finite element analysis (FEA) considered interactions between cell pressures and face deformation. Periodic boundary conditions were applied to a small representative volume element. In uniaxial, biaxial and triaxial tensile stress states, the dominant high-strain deformation mechanism was predicted to be tensile yield across nearly flat faces. In uniaxial and biaxial compression stress states, pairs of parallel plastic hinges were predicted to form across some faces, allowing them to concertina. In hydrostatic compression, face bowing was predicted. The rate of post-yield hardening changed if new deformation mechanisms became active as the foam strain increased. The effects of foam density and polymer type on the foam yield surface were investigated. Improvements were suggested for foam material models in the FEA package ABAQUS.

Introduction

Closed-cell, low-density polymer foams are used in personal protective equipment and the packaging of goods in transit [1]. The polymers used are either glassy, with Young's moduli of about 3 GPa, such as polystyrene (PS), or semi-crystalline with Young's moduli ranging from 0.1 to 1 GPa, such as polyethylene (PE). PS foam impact protection is invariably expanded polystyrene (EPS), fabricated using the bead moulding process (see Chapter 4 of [1]). The beads in any particular EPS moulding have a distribution of density, hence of mechanical properties; similar distributions were quantified, and followed during foam compression, in expanded polypropylene (EPP) [2]. The bead-level microstructure of EPS will not be considered here; the small void content between beads in EPP is not predicted to significantly reduce the foam yield stress [3], although it reduces the compressive Young's modulus.

When the foam relative density R (the foam density divided by the polymer density) is less than 0.08, the microstructure typically consists of polyhedral, thin-walled cells with mean diameters in the range from 0.1 to 1 mm. When $R \cong 0.02$, the cell edges are of similar thickness to the faces, and the foams can be described as *dry*. This nomenclature derives from soap froths, where the initially *wet* foams have edges that are much thicker than the faces. As water drains from the froth, it tends towards a dry state.

Polymer foams have a range of cell sizes and shapes, hence irregular cell packing. Models of disordered foams [4] contain too many cells (>400) for FEA to be able to predict the yield surface. Therefore, modellers have often considered foams with uniform-sized cells on a regular lattice, such as the so-called Kelvin foam [5] and the Weaire–Phelan foam [6], which are nearly isotropic. The former, with Body Centred Cubic (BCC) symmetry and a smaller unit cell, is more often used. The cell faces in the dry Kelvin foam are flat, whereas Lord Kelvin [7] proposed a minimum surface area structure for soap froths that contained slightly curved hexagonal faces. The identical cells have eight hexagonal faces and six square faces, whereas polymer foams contain a statistical distribution of 4-, 5-, 6- and 7-sided faces. The Kelvin foam Young's modulus anisotropy is 8% [8], while that of its uniaxial compression initial yield stress was between 1 and 9% [9].

N. J. Mills (✉)
Metallurgy and Materials, University of Birmingham, Birmingham B15 2TT, UK
e-mail: n.j.mills@bham.ac.uk

Permanent folding of cell faces, by the formation of parallel 'plastic hinges' across faces, has been observed in EPS foams after uniaxial compressive impact [9]. A dry Kelvin foam model [9] predicted this mechanism, and the uniaxial-compression stress–strain impact response of foam sheets, up to six cells thick, based on PS and low-density polyethylene (LDPE). A refinement of the dry Kelvin model, using periodic boundary conditions on a representative volume element (RVE) from an infinite foam, gave the same stress–strain predictions within 5% [10] for compression in the [111] direction. It predicted that deformation was inhomogeneous on a cell size scale. However, EPS foam, with a disordered microstructure, deforms homogenously on a scale >1 mm when compressed uniaxially [11]. The predicted compression yield stress [10] of a wet Kelvin model of LDPE foam, with 25% of the polymer in the edges, and a relative foam density of 0.048, was 18% lower than that of the equivalent dry Kelvin foam. The difference is expected to be minimal if less than 5% of the polymer is in the foam edges.

The only published prediction, of the deformation mechanisms of closed-cell polymer foams under stress states other than uniaxial compression, is that of Gibson et al. [12] who analysed an open-cell foam model with simple cubic cells, and then applied the predictions to both open- and closed-cell foams. However, their cell geometry differed markedly from that of polymer foams, and the open-cell models should not be applied to closed-cell foams. Therefore, although the dry Kelvin foam is slightly anisotropic, it will be used here to model foam yield under multi-axial stresses. A similar model was used to predict the yield surface of closed-cell aluminium foam [13]; in a 2D plot, the ellipse diameter along the hydrostatic pressure axis was four times that along the deviatoric stress axis. As the 70 GPa Young's modulus of aluminium greatly exceeds that of polymers, and the aluminium foam relative density was 0.1, face buckling was unlikely prior to yield. Consequently, this yield surface is unlikely to apply to polymer foams.

A yield surface in a 3D space using the principal stresses as axes describes the multi-axial stresses that cause a material to yield. Foam yield surfaces often have simple convex shapes [14], rather than being based on models of foam deformation mechanisms. If the surface has axial symmetry about the hydrostatic stress axis, then it can be described by a 2D plot of the hydrostatic pressure component p versus the von-Mises-equivalent deviatoric stress component σ_e. These quantities are defined in terms of the principal stresses σ_i as

$$p = -\frac{1}{3}(\sigma_1 + \sigma_2 + \sigma_3) \quad (1)$$

$$2\sigma_e^2 = (\sigma_1 - \sigma_2)^2 + (\sigma_2 - \sigma_3)^2 + (\sigma_1 - \sigma_3)^2 \quad (2)$$

The yield surfaces of some low-density polymer foams have been determined, from a discrete number of points. Data for Divinylcell (a mixture of rigid PVC and an interpenetrating polymer network) closed-cell foams of nominal densities 100 and 200 kg m^{-3} was fitted with a quadratic yield criterion, capped by a compressive principal stress criterion [15]. EPS of very low 16 kg m^{-3} density was studied in stress states close to hydrostatic compression [16]; the yield surface in the π plane, perpendicular to the hydrostatic axis, was circular with a radius that decreased as p increased from 0.12 to 0.18 MPa.

FEA has been used to predict the impact performance of products made from polymer foams, e.g. protective helmets [17, 18]. The FEA package ABAQUS [19] contains a *crushable foam* material model; its yield surface for polymer foams hardens as the foam volume changes. It requires an input of uniaxial compressive stress–strain data, the ratio p_t/p_{C0} of the initial yield pressures in hydrostatic tension and compression, respectively, and σ_{C0}/p_{C0}, where σ_{C0} is the initial yield stress in uniaxial compression. The ABAQUS manual suggests using p_t/p_{C0} between 0.05 and 0.1, without giving any justification. It is almost impossible to measure p_t because the sudden application of a vacuum to polymer foams does not cause yield. Figure 1 shows the yield surface [20] for extruded (slightly anisotropic) polystyrene foam of density 35 kg m^{-3} using limited experimental data, and assuming $p_t/p_{C0} = 1.0$ and $\sigma_{C0}/p_{C0} = 1.933$.

As all polymer mechanical properties are strain-rate dependent to some extent, foam properties should be measured at high strain rates for use in impact modelling.

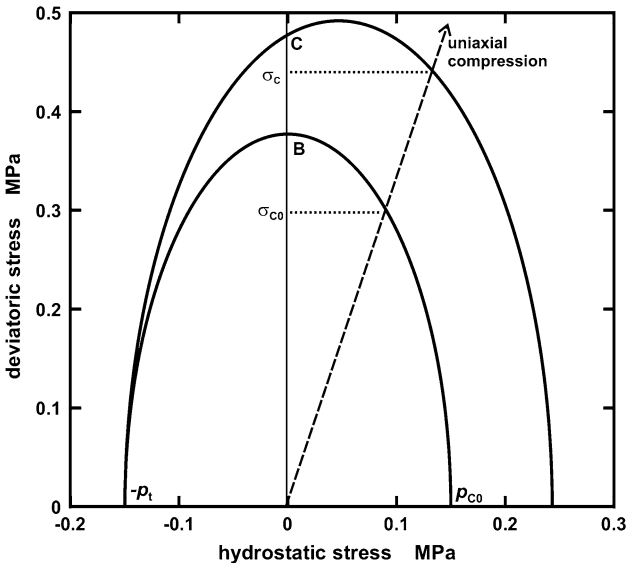

Fig. 1 Deviatoric stress component versus hydrostatic stress component; initial and hardened yield surfaces for PS foam of density 35 kg m^{-3} [20]

Foam uniaxial compressive responses can be measured at impact strain rates, but p_{C0} can only be measured at strain rates the order of 1 s^{-1}. The foam material model in ABAQUS does not harden in simple shear deformation, as the foam volume is constant; however experiments show [20] that EPS hardens in simple shear. Therefore, a micromechanics model of the yield surface of PS foam would aid the interpolation of limited experimental data, and suggest reasonable values of p_t/p_{C0}. Predictions of hardening would assist the development of a better foam material model.

The aims are, therefore, to predict the yield surfaces of typical low-density polymer foams, their hardening after yield in various stress states, and the dominant deformation mechanisms. Hopefully, the latter can be confirmed by microscopy of deformed specimens.

Foam model

Multiaxial stress (strain) states

The multi-axial stress states modelled were chosen to correspond, as far as possible, with those commonly used in experiments. In hydrostatic compression experiments, a time-varying hydrostatic pressure is applied to a foam specimen inside a closed chamber; as the foam shape is not constrained, the strains may not be uniform. Table 1 gives the *strain ratios*, the ratios of the principal strains in the foam, where 123 are the principal axes. The zeros in Table 1 indicate zero stress components. Hence, for uniaxial tests, in which the unconstrained side surfaces of the specimens are stress free, the table gives the ratio of principal stresses.

Two directions of uniaxial compression were modelled to check the isotropy of the RVE. The 'pure shear' state initially has a zero hydrostatic pressure component p, as $\sigma_1 = -\sigma_2$ and $\sigma_3 = 0$; however, after plastic deformation, the structure becomes anisotropic and p becomes non-zero.

The dry Kelvin foam model, and the RVE symmetry

The high symmetry of the Kelvin foam allows a small RVE to be analysed [9, 10]. Periodic boundary conditions at the RVE boundaries, or mirror boundary conditions on a rectangular cuboid RVE, allow it to represent an infinite foam. A dry Kelvin foam model [9] was used to consider foams of low relative density. The foam geometry was, for convenience, generated using Surface Evolver [21] software. The cell diameter $D = 1$ mm was within the range of mean cell size for commercial foams. Cell size has no effect on the foam mechanical properties, and very little on the heat transfer rate during impact compression for this size range. The foam relative density R (Table 2) was varied over the lower part of the commercial range, by using two values of face thickness. Foams with $R > 0.05$ are often better represented by a wet Kelvin model.

The RVE was a rectangular cuboid, with its 2 axis aligned with the lattice [010] direction, so the three principal strains could be varied independently. This would not be possible for a triangular-prism RVE aligned with the lattice [111] direction. The RVE had height $2D$, and width and depth $D/\sqrt{2}$ (Fig. 2). Its 1 and 3 axes lie at 45° to the [100] and [001] axes of the BCC lattice. Chains of corner-to-corner linked square faces lie along each of the BCC lattice $\langle 001 \rangle$ type axes. Consequently, type 'A' vertices along the RVE central vertical [010] axis are contacted by faces having a particular set of orientations relative to the principal stress axes. Type 'B' vertices are contacted by faces having a different set of orientations. The two-cell high RVE allows volume strains to differ in neighbouring

Table 2 Kelvin model, for foams of cell diameter $D = 1$ mm

Face thickness (μm)	Foam relative density (R)	LDPE foam density (kg m^{-3})	PS foam density (kg m^{-3})
7	0.0234	21.6	24.6
14	0.0467	43.1	49.2

Table 1 'Test' conditions for yield surface evaluation

Strain (* stress) state	Abbreviation	Strain (stress) ratios		
		Axis 1	Axis 2	Axis 3
Hydrostatic compression	HC	−1	−1	−1
Biaxial compression in 12 plane	BC12	−1	−1	0
*Uniaxial compression along 2 axis	C2	0	−1	0
*Uniaxial compression along 1 axis	C1	−1	0	0
Pure shear in 12 plane	PS12	−1	1	0
*Uniaxial tension along 2 axis	T2	0	1	0
Biaxial tension in 12 plane	BT12	1	1	0
Hydrostatic tension	HT	1	1	1

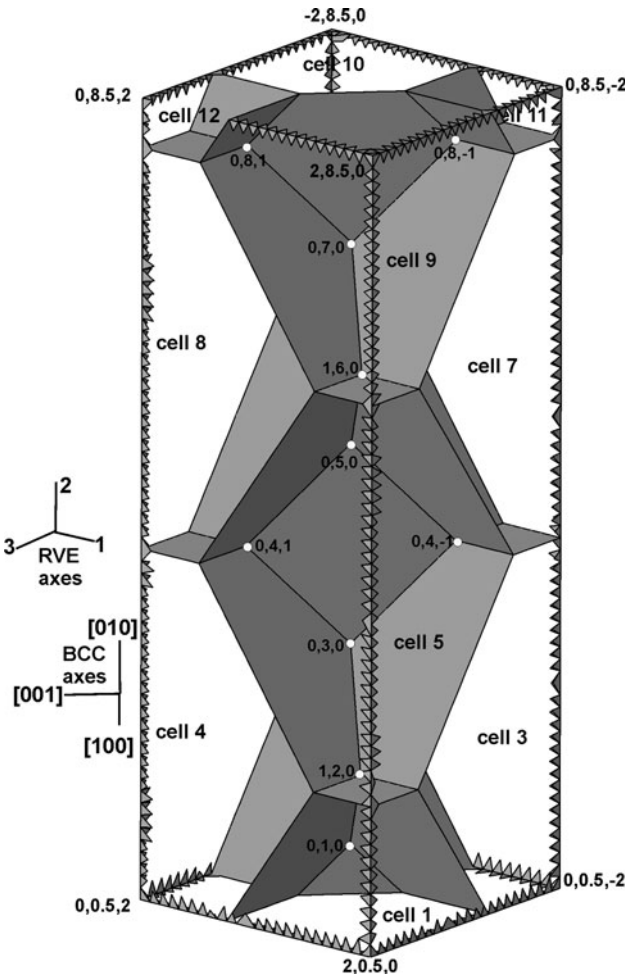

Fig. 2 Two-cell high dry Kelvin foam RVE, with cells numbered. The BCC coordinates of the vertices (*white circles*) and RVE corners are given in units of ¼: type 'A' vertices have coordinates (0, *x*, 0), the others are type 'B'. For clarity, the membrane faces at all the RVE external surfaces are omitted. All the models are viewed without perspective

cells, but not long-range inhomogeneity. If a ten-cell high RVE were used, then it would overemphasise strain localisation in the foam under uniaxial compression; this only occurs in such regular cell models [9], and not in the irregular structures of real polymer foams.

None of the RVE boundary surfaces contains foam cell faces, so all these faces can buckle under in-plane compression, and bow if subjected to pressure difference. A foam face that lay in a mirror-symmetry RVE boundary, or was pressed against a flat anvil, would be constrained to remain flat; hence, the model might excessively resist multi-axial compressive deformation.

The undeformed and deformed lattices have mirror symmetry at the four side external surfaces of the RVE. Hence, the foam cell faces, where they meet the RVE sides, remain perpendicular to these sides. The deformation pattern of the polymer structure should have periodic symmetry along the RVE 2 axis; equations stated that the in-plane (1 and 3 axis) displacements and three rotations were equal at corresponding nodes on the RVE top and base. However, it was not possible to successfully implement in ABAQUS Explicit a condition that the 2 axis displacement of each top surface node equalled that of the corresponding base node plus a constant. With such a condition, computation of the foam stress in the 2 direction would be difficult. Consequently, the 2-axis displacements were over-constrained by enforcing contact with a rigid table. This approximation of full periodicity constrained the deformation of 'sloping' faces of small cells 11 and 12 at the top of the RVE (Fig. 2) in hydrostatic and biaxial compression. As these cells only comprise 1/16th of the RVE height, there was only a minor effect on the overall RVE strain.

Air-filled cells and meshing

The treatment of foam cells in ABAQUS models has been described [9, 10]. The approach is outlined here, with details given when different from previous modelling.

The RVE does not contain any complete cells from the Kelvin foam, but only 12 partial cells. The six external surfaces of the RVE were incorporated into the FEA part (Fig. 2), so each partial cell had a closed surface and a defined volume. These surfaces were modelled with 0.1-μm thick membrane elements of a very low shear modulus (10 kPa) hyperelastic material, and so they do not contribute to the mechanical resistance of the structure. They run through the centres of complete cells, and remain flat. Hence, the pressures in the two parts of the complete cell are equal. The 12 partial cells were *surface-based fluid cavities* with meshed surfaces but unmeshed air-filled volumes. The pressures in each pair of cells (1 and 9, 2 and 10, 3 and 11, and 4 and 12) were kept identical by a *fluid exchange* function of a suitable connecting 'pipe'. Consequently, the cell pressures were periodic along the RVE 2 axis, with a repeat distance of 2*D*.

The cell air was assumed to be an ideal gas, initially at atmospheric pressure. It remained at ambient temperature during deformation, because of rapid heat transfer to the polymer faces, of larger thermal capacity. If deformed cell faces contact, then the friction coefficient was zero. The parts were meshed using a seed size of 30 μm, with linear shell elements in the cell faces, triangular membrane elements in the symmetry surfaces, and rigid elements in the constraining planes.

Material properties

Since no mechanical property data was available for the biaxially stretched faces of PS and LDPE foam, it was

necessary to use tensile stress–strain data from biaxially drawn polymer films [9]. True-stress versus true-strain data for tensile tests on 5.5 times biaxially drawn polystyrene (PS) film was fitted with a yield stress $\sigma_Y = 73$ MPa and ideal plastic behaviour (constant yield stress). The PS density $\rho = 1050$ kg m^{-3}, Young's modulus $E = 3.0$ GPa and Poisson's ratio $v = 0.4$. The material properties were taken as strain-rate independent.

For 6.5 times biaxially drawn LDPE film, true-stress versus true-strain data, for tensile tests with a strain rate of ca. 50 s^{-1}, was fitted with a bilinear relationship; the true yield stress was initially $\sigma_Y = 12$ MPa, it increased linearly to 18 MPa at a true plastic strain of 0.26, and then to 48 MPa at a true strain of 0.67. The other material constants were $\rho = 920$ kg m^{-3}, $E = 0.20$ GPa and $v = 0.4$.

Boundary conditions on the RVE and stress determination

In order to impose multi-axial strains on the RVE, its exterior surfaces underwent frictionless contact with an appropriate number of rigid planar tables; six for hydrostatic deformation, four for biaxial deformation, and two for uniaxial deformation. One of each pair of tables was fixed (encastré). The other moved in (or out) and remained parallel. It initially contacted the RVE at zero velocity, to minimise initial force oscillations, but its velocity rapidly increased to a near-constant value causing a strain rate of 100 s^{-1}, typical of a drop weight impact test.

For uniaxial and biaxial tests, the stress-free surfaces were constrained so that the RVE remained a rectangular prism. Mirror-symmetry boundary conditions were directly implemented in ABAQUS explicit.

The engineering stresses in the foam (principal stresses, representing the average stress acting on the RVE) were calculated from the reaction forces F using

$$\sigma_{11} = \frac{F_1}{\sqrt{2}D^2} \quad \sigma_{22} = \frac{2F_2}{D^2} \quad \sigma_{33} = \frac{F_3}{\sqrt{2}D^2} \tag{3}$$

where the force component F_i acts along the i axis on the fixed table that is normal to that axis. The engineering strains in the foam (principal strains, representing the average strain in the RVE) were calculated from the displacements of the moving tables

$$e_{11} = \frac{\sqrt{2}U_1}{D} \quad e_{22} = \frac{U_2}{2D} \quad e_{33} = \frac{\sqrt{2}U_3}{D} \tag{4}$$

where U_i is the i axis displacement of the table that moves along the i axis

Predictions

Deformation mechanisms

The following definitions were used: *initial yield* occurred when the von-Mises-equivalent true plastic strain (the variable PEEQ in ABAQUS) first reached 0.01 at any location in the structure; *foam yield* occurred when a continuous yielded zone with PEEQ ≥ 0.01 crossed the foam structure, causing the stress–strain relationship to change slope, or the stress to reach a maximum. Buckling modes are shown in Fig. 3; the mode number is one plus the number of changes of sign of the face curvature along the cut edge.

Deformation mechanisms were predicted for PS foam of density 49 kg m^{-3} (PS49) for the following deformation modes. Deformation mechanisms for other foams, if different, are mentioned in "Stress–strain responses for PS foam of density 25 kg m^{-3}" and "Stress–strain responses for LDPE foam of density 43 kg m^{-3}" sections.

Hydrostatic compression

The hexagonal cell faces first buckled elastically, in mode 1, when the foam strains $e_i = -0.2\%$ ($i = 1, 2, 3$). Initial yielding occurred near, and parallel to, about half of the cell edges, at foam strains $e_i = -0.8\%$. The foam yielded at $e_i = -2.3\%$ when the plasticity spread around most of the periphery of the faces (Fig. 4). The cut edges, visible at the sides of the RVE, rotated, but not all in the same direction. The arrowed sloping face, between cells 1 and 4 at the left, had an opposite curvature to its 'continuation' in the arrowed small sloping face, between cells 9 and 12, at the right of the figure, an anomaly due to the approximation of periodic boundary conditions. Nevertheless, the major parts of the cell faces bowed freely, with a magnitude that

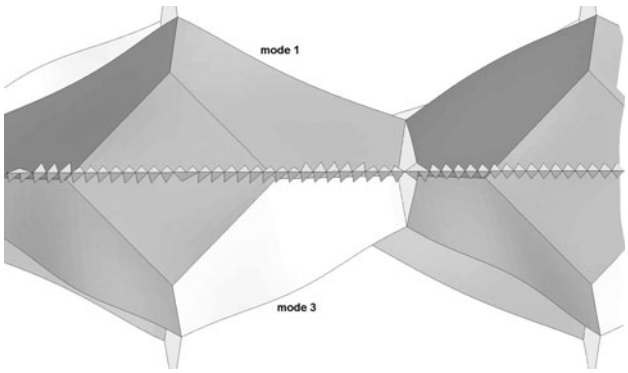

Fig. 3 Modes of elastic face buckling, shown in biaxially compressed PS49 foam at strains −0.9%, −0.9% and 1.4%

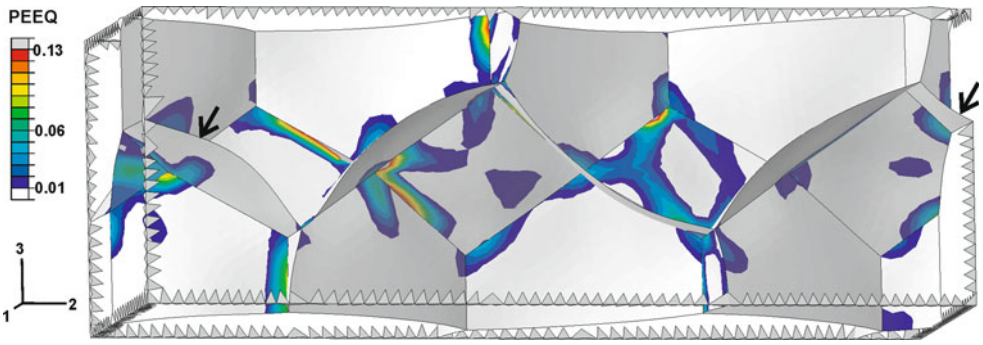

Fig. 4 Contours of equivalent plastic strain PEEQ in hydrostatically compressed PS49 at initial foam yield at $e_i = -2.3\%$

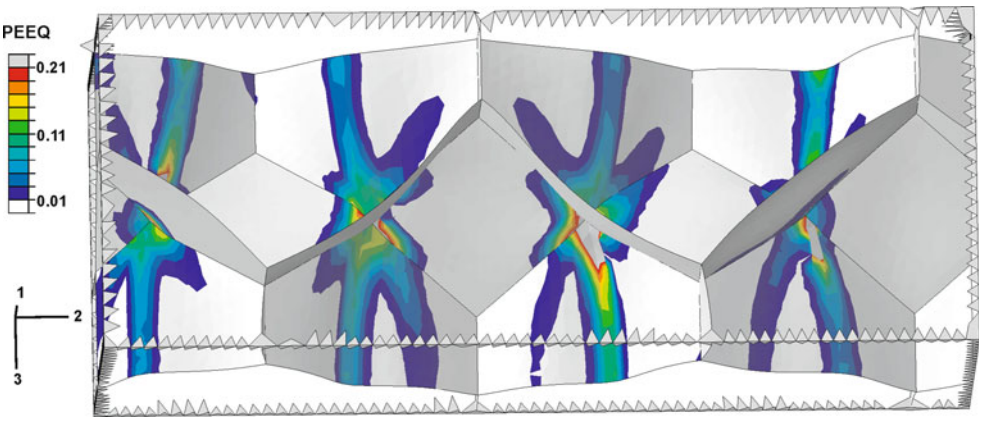

Fig. 5 Contours of equivalent plastic strain in biaxially compressed PS49 at initial foam yield at $e_1 = e_2 = -4.1\%$. Hexagonal faces containing the 3 axis fold into three sections at parallel plastic hinges

increased with foam strain. At the maximum strain of the simulation $e_i = -15.7\%$, plasticity had spread across the square faces. The bowing of hexagonal faces was aided by yielding near edges, but plasticity did not reach the centres of faces.

Biaxial compression

Hexagonal faces buckled elastically in modes 1 and 3 at foam strains $e_1 = e_2 = -0.6\%$, and the initial localised yielding occurred at $e_1 = e_2 = -1.1\%$. When $e_1 = e_2 = -2.1\%$, each hexagonal face that initially contains the 3 axis developed a plastic hinge across its centre and the foam yielded. At $e_1 = e_2 = -4.1\%$ and $e_3 = 5.8\%$, these hexagonal faces concertinaed, with two parallel plastic hinges separating three elastic sections (Fig. 5). The hexagonal faces that initially contained the 1 axis remained largely elastic, but some eventually folded slightly. Therefore, only one set of hexagonal faces underwent a face-folding mechanism, and the cell deformation was relatively homogeneous.

Uniaxial compression

The deformation mechanisms were similar to those described before [9, 10]. Modes 1 and 2 elastic buckling occurred in hexagonal faces at $e_2 = -1.6\%$. At $e_2 = -2.5\%$ yield initiated in horizontal bands across the centres of the square faces containing the 2 axis, and these faces became slightly bowed. Single horizontal plastic hinges, meeting at a type 'A' vertex, formed across the centres of four hexagonal faces at a foam strain $e_2 = -2.5\%$. The foam yielded when the compressive stress reached a maximum; a second plastic hinge formed higher in each face, parallel to the first hinge, at a foam strain $e_2 = -4.2\%$ (Fig. 6). The faces concertinaed at one height in the model, with some associated yield in the touching vertical square face. This plastic collapse was more drastic than in biaxial compression, and the sudden stress drop (see "Stress–strain responses of PS foam of density 49 kg m^{-3}" section) was due to the cell deformation becoming inhomogeneous. This was the only stress state that caused such a macroscopic strain inhomogeneity. Another set of linked hexagonal faces collapsed in a similar manner, at a different height in the model, at a foam strain $e_2 = -34\%$.

Pure shear

No elastic buckling occurred prior to yield in this or the following three stress states. Yield initiated at type 'A' vertices at $-e_1 = e_2 = 1.6\%$. The foam yielded at $-e_1 = e_2 = 2.6\%$ when the plasticity spread into a wavy band across the square faces between these vertices. At $-e_1 = e_2 = 4.1\%$, these faces concertinaed into three

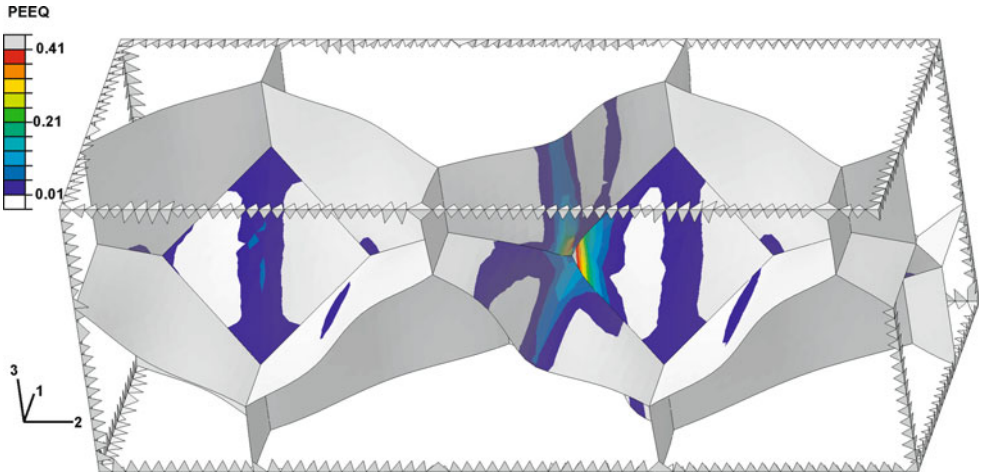

Fig. 6 Contours of equivalent plastic strain in uniaxial-compressed PS49 foam at initial foam yield when $e_2 = -4.2\%$. Four linked hexagonal faces, at one level in the model, each fold into three sections at parallel plastic hinges

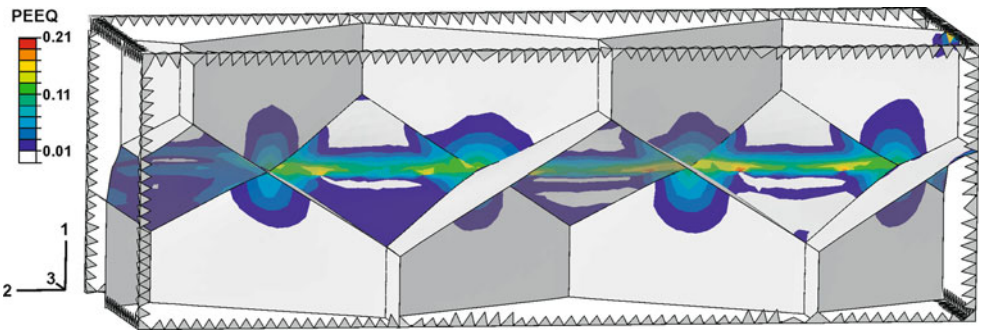

Fig. 7 Contours of equivalent plastic strain in PS49 under pure shear at $e_1 = -4.1\%$, $e_2 = 4.1\%$: 'vertical' square faces fold into three sections at parallel plastic hinges, while hexagonal faces containing the 1 axis begin to stretch across their centres

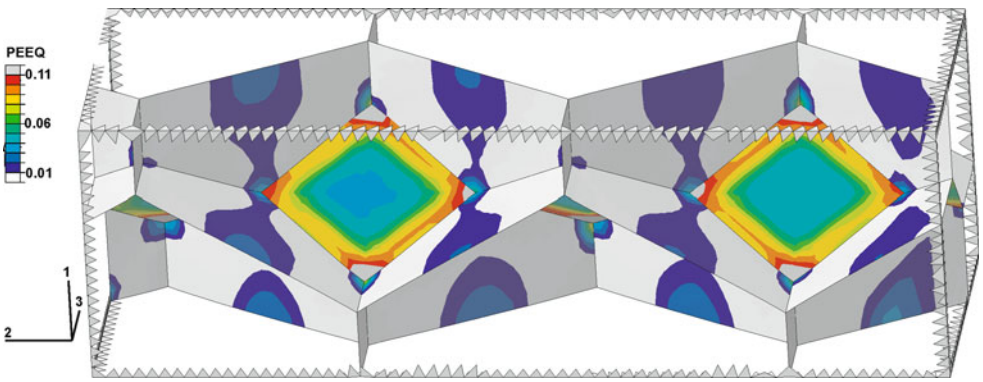

Fig. 8 Contours of equivalent plastic strain in PS49 under uniaxial tension at $e_2 = 7.9\%$. Vertical square faces have yielded, and hexagonal faces have yielded across their centres

sections, with plastic hinges parallel to the 2 axis (Fig. 7). At strains $-e_1 = e_2 = 9.7\%$, the plasticity had spread in a broad band across the hexagonal faces that contain the compressive 1 axis; these faces yielded in tension, in a diffuse band across their centres, but remained flat.

Uniaxial tension

Yield initiated at the vertices, at $e_2 = 2.3\%$. The foam yielded at $e_2 = 3.1\%$ when plasticity spread around the peripheries of square faces that link the type 'A' vertices. These square faces became fully plastic by $e_2 = 4.4\%$. At $e_2 = 7.5\%$ (Fig. 8) the yielded zone had spread across the structure. At $e_2 = 22\%$, these square faces contained wrinkles parallel to the 2 axis, as in the plane strain case.

Biaxial tension

Yield initiated at the type 'A' vertices, at $e_1 = e_2 = 1.2\%$. The foam yielded at $e_1 = e_2 = 2.8\%$ when bands of plasticity spread from these vertices right across the centres of the hexagonal faces that contain the 3 axis ($\sigma_3 = 0$) (Fig. 9). At this stage, all the faces were flat. At $e_1 = e_2 = 5.5\%$, diffuse tensile necks developed across

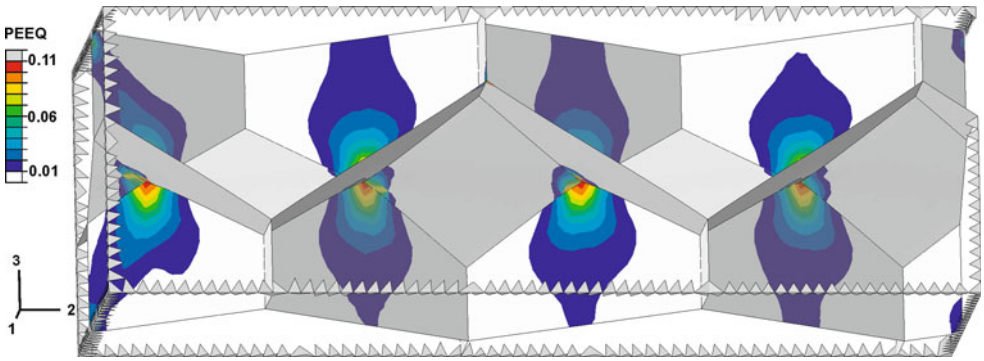

Fig. 9 Contours of equivalent plastic strain in PS49 under biaxial tension at initial foam yield at $e_1 = e_2 = 2.8\%$. Tensile yield has spread across hexagonal faces containing the 3 axis

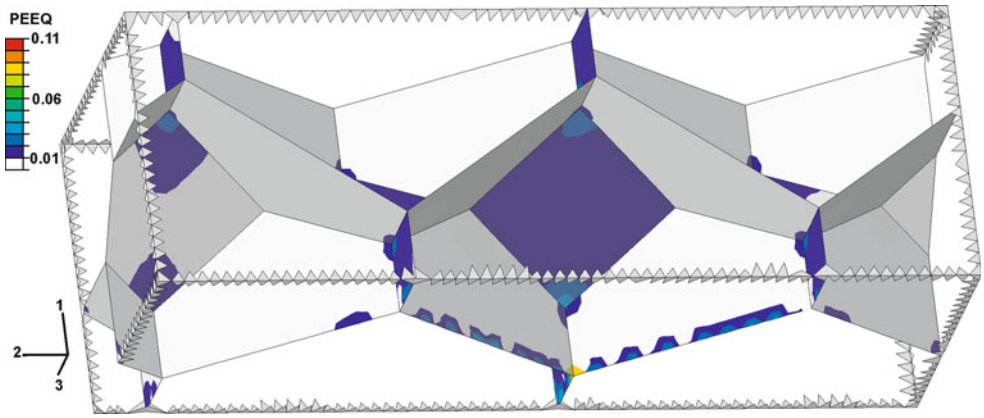

Fig. 10 Contours of equivalent plastic strain in PS49 under hydrostatic tension at initial foam yield when $e_i = 1.9\%$

these hexagonal faces, while the hexagonal faces containing the 1 axis became slightly bent, as in mode 2 buckling. Above this foam strain level, the plastic strains increased in the necks.

Hydrostatic tension

The foam cell faces remained flat prior to yield. Plasticity initiated in the square faces at $e_i = 1.6\%$. The foam yielded when these faces became fully plastic at $e_i = 1.9\%$ (Fig. 10); the plastic strain was greater in the square faces than in the hexagonal faces, in spite of the uniform hydrostatic strain applied to the foam. Linked tensile necks formed across the top of the structure at $e_i = 5.1\%$, causing the stress to drop suddenly.

Stress–strain responses of PS foam of density 49 kg m^{-3}

Figure 11 compares the stress–strain responses of PS49 with PS foam of density 25 kg m^{-3} (PS25) and LDPE foam of density 43 kg m^{-3} (PE43); the latter has the same relative density as PS49. The stresses for the PS25 foam were doubled, and those for PE43 foam multiplied by six, to assist visual comparison; their responses are described later.

The foam initial yield stress (Table 3) was the highest for hydrostatic tension, and the lowest for biaxial compression. The hydrostatic tension value ($\sigma_i = 2.25 \pm 0.03$ MPa) was the highest because all the faces yielded simultaneously, under in-plane principal stresses that were both tensile. In biaxial tension, only one set of hexagonal faces yielded, with a compressive principal stress, acting close to the edge of these faces, assisting the process. The hydrostatic tension yield stress is related to the polystyrene yield stress ($\sigma_0 = 73$ MPa) and the foam relative density R (Table 2) by $0.66\sigma_0 R$, showing that the plastic strain in the RVE is not uniform (if it were, then the constant should be 1.0). The bulk modulus K was 141 MPa for the linear pre-yield response in hydrostatic tension; hence, in terms of the polymer Young's modulus E and the foam relative density R, it is given by

$$K = 1.0ER \tag{5}$$

It was difficult to compare post-yield hardening or softening quantitatively, because the maximum strains reached were a function of the stress state. The softening was approximately the same for hydrostatic and biaxial compressive stress states, which cause homogeneous deformation on a cell-size scale. In hydrostatic compression (Fig. 11a), the three principal stresses (almost equal) fell gradually as the amplitude of face bowing increased. The biaxial stress–strain relationships (Fig. 11b) are very similar, in spite of the deformation mechanism changing. However, for uniaxial compression along the 2 axis

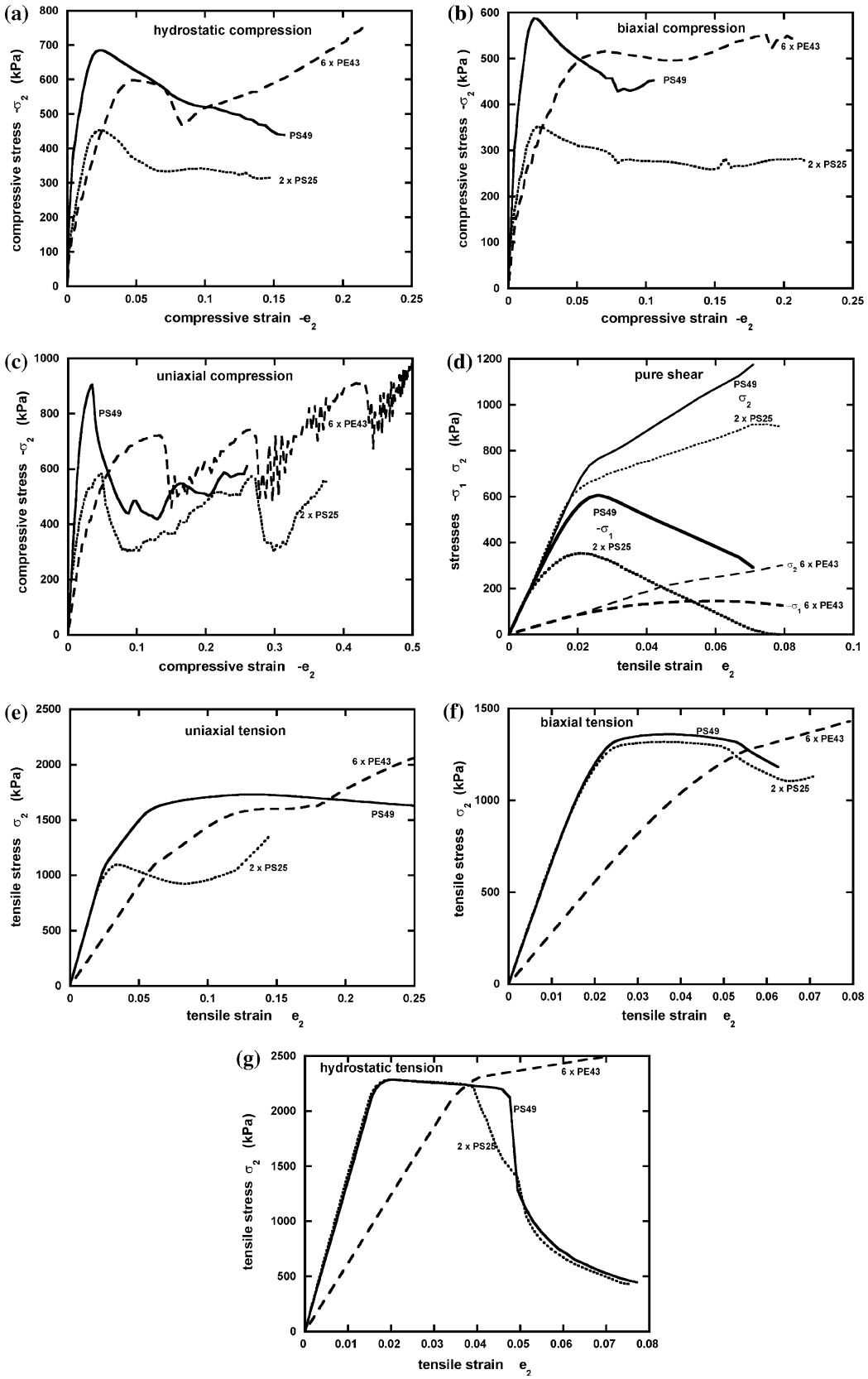

Fig. 11 Engineering stress–strain responses for **a** hydrostatic compression, **b** biaxial compression, **c** uniaxial compression, **d** pure shear, **e** uniaxial tension, **f** biaxial tension and **g** hydrostatic tension. Stresses for PS25 and PE43 are magnified to make comparison easier

Table 3 Predictions for PS foam of density 49 kg m^{-3}

Stress state	Initial yield stress (kPa)			Yield strain e_2 (%)	When e_2 is (%)	Free strains are (%)	
	σ_{01}	σ_{02}	σ_{03}			e_1	e_3
HC	−692	−685	−694	−2.3			
BC12	−608	−588	0	−2.1	−10	–	11.7
C2	0	−905	0	−2.5	−10	0.5	0.5
C1	−940	0	0	−4.1	$e_1 = -10$	$e_2 = -0.1$	6.4
PS12	−606	765	0	2.6	7.1	–	2.2
T2	0	1110	0	3.1	10	−4.2	−4.2
BT12	1400	1340	0	2.8	6.2	–	−8.2
HT	2220	2280	2220	1.9			

Table 4 Predictions for PS foam of density 25 kg m^{-3}

Stress state	Initial yield stresses (kPa)			σ_{02} ratio PS25/PS49	e_2 yield (%)
	σ_{01}	σ_{02}	σ_{03}		
HC	−229	−227	−227	0.33	−1.9
BC12	−219	−176	0	0.30	−2.3
C2	0	−292	0	0.32	−4.7
C1	−303	0	0	0.32[a]	4.1
PS12	−177	320	0	0.29[a], 0.42	2.1[b]
T2	0	550	0	0.50	3.4
BT12	600	630	0	0.47	2.3
HT	1120	1140	1120	0.49	1.9

[a] Comparison of σ_{01}

[b] At maximum σ_1

(Fig. 11c), sudden softening occurred when plastic hinges formed across a quartet of hexagonal faces. The structure hardened again, prior to the collapse of a set of linked faces at a different height in the model.

In pure shear (Fig. 11d), the compressive stress $-\sigma_1$ reached a maximum at the initial foam yield, as some faces began to concertina. However, the slope of the tensile stress σ_2 graph remained positive, as other stretched faces aligned towards the tensile axis. At high strains, the geometric nonlinearity of the structure causes the stresses $-\sigma_1$ and σ_2 to diverge, and so the hydrostatic pressure component p becomes non-zero.

For uniaxial tension (Fig. 11e), the slope of the graph decreased when the foam yielded at 3.1% strain, and again when another plasticity mechanism became active at 5% strain. For biaxial tension (Fig. 11f), the slope of the graph became zero after foam yield, and then negative when tensile necks formed across the structure. The tensile stress σ_1 was within 5% of σ_2 in the post-yield region. For biaxial and hydrostatic tensions (Fig. 11f, g), the foam stress remained almost constant for a while after foam yield, due to the lack of tensile post-yield hardening in the polystyrene. Later, diffuse necking in biaxial tension caused softening. In hydrostatic tension, localised necking caused a more pronounced softening, and the deformation in the RVE eventually became inhomogeneous. The free lateral strains (Table 3) were small at $e_2 = 10\%$ for uniaxial compression along the 2 axis, due to the cell faces concertinaing. However, they were large in the biaxial stress modes.

Stress–strain responses for PS foam of density 25 kg m^{-3}

The yield stresses for PS25 foam, in the eight deformation modes, are presented in Table 4, together with the ratio of the initial yield stress σ_{02} to that of PS49. Halving the foam density caused the initial yield stresses for tensile-loading modes (hydrostatic, biaxial and uniaxial) to halve, showing that they are proportional to the foam relative density R. However, the effect for compressive modes (hydrostatic, biaxial and uniaxial) was to multiply the initial yield stress by a factor close to $1/2\sqrt{2} = 0.35$, suggesting that they are proportional to $R^{1.5}$. For pure shear loading, the tensile principal stress at yield was almost proportional to R, while the compressive principal stress was significantly smaller.

The shapes of the stress–strain graphs for PS25 foam (Fig. 11) were very similar to those for PS49 foam. The exception is uniaxial tensile loading; wrinkles formed in the thinner PS25 foam faces, in square faces between type

Table 5 Predictions for LDPE foam of density 43 kg m^{-3}

Stress state	Initial yield stresses (kPa)			σ_{02} ratio PE43/PS49	Yield strain e_2 (%)
	σ_{01}	σ_{02}	σ_{03}		
HC	−99	−100	−101	0.146	−4.8
BC12	−87	−86	0	0.146	−7.1
C2	0	−116	0	0.128	−10.2
C1	−121	0	0	0.129[a]	−10.2
PS12	−78	128	0	0.129[a], 0.167	6.3
T2	0	270	0	0.243	13.0
BT12	225	215	0	0.161[a], 0.160	5.5
HT	380	380	380	0.167	3.9

[a] Comparison of σ_{01}

'A' vertices, parallel to the tensile stress 2 axis. This relieved the compressive stresses across these faces, and altered the sites for further plasticity.

Stress–strain responses for LDPE foam of density 43 kg m^{-3}

The eight deformation modes were simulated for PE43 foam, having the same relative density as PS49. As polystyrene has 15 times the Young's modulus of LDPE, but six times the initial yield stress, the yield strain in the LDPE is approximately double that in PS. Consequently, the yield strains of PE43 foam were nearly double those of PS49, for the same stress state. The PE43 foam initial yield stresses (Table 5) were approximately one-seventh of those of PS49 for the three compressive stress states, but approximately one-sixth for the three tensile stress states. When the foam yield mechanism was face tensile yield, the foam yield stress depended on the polymer yield stress. In the tensile simulation, the first stage of yielding was observed at a

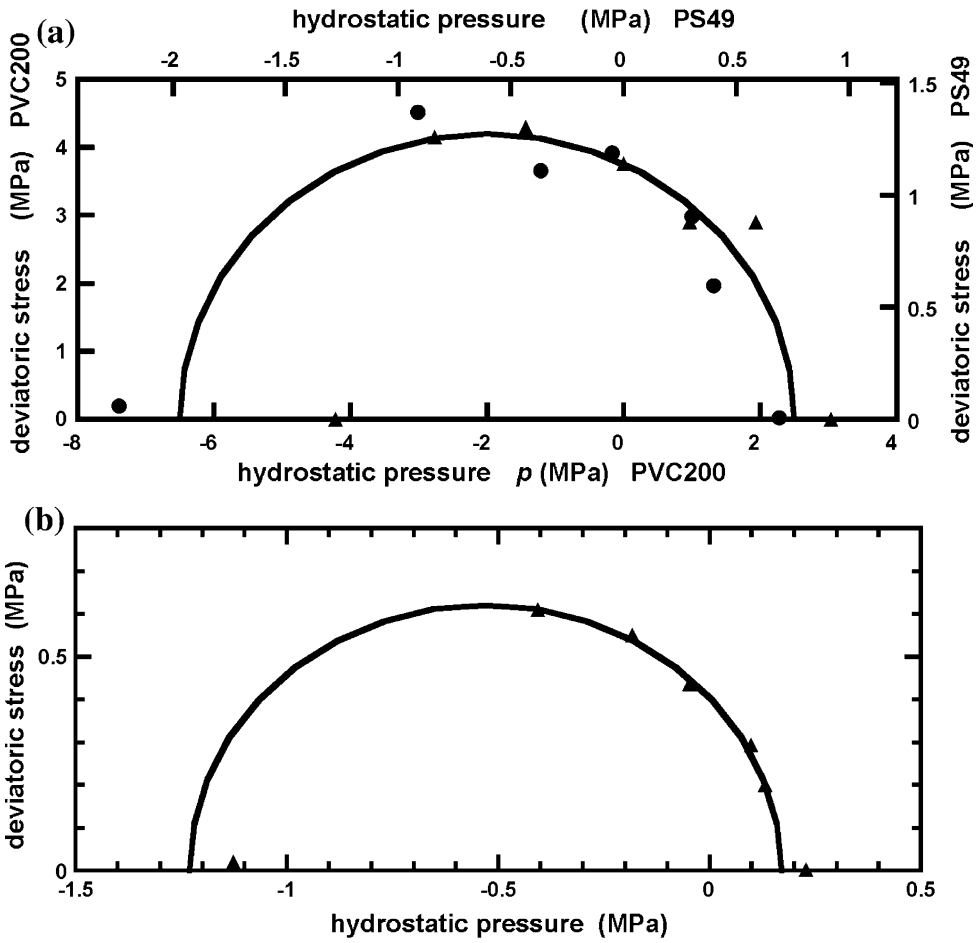

Fig. 12 Yield surfaces: **a** predictions for PS49 foam (*circles*) cf experimental data (*triangles*) for PVC foam of density 200 kg m^{-3} [15] fitted with Eq. 6, **b** predictions for PS25 foam, fitted with an ellipse

Table 6 Parameters of yield surface ellipses

Foam	Deviatoric stress diameter (MPa)	Hydrostatic stress diameter (MPa)	Centre (MPa)	Axial ratio deviat/hydro
PS49	2.54	2.72	−0.61	0.93
PS25	1.24	1.40	−0.53	0.89
LDPE43	0.44	0.44	−0.15	1.0

180 kPa stress (6% strain), but complete yielding did not occur until a significantly higher stress was reached.

Pressure differences between cells caused greater face deformation in PE43 foam than in the stiffer PS49 foam. Consequently, in uniaxial compression of PE43 foam, there were cell volume changes on a short time scale driven by face elasticity, revealed as stress oscillations over a small strain range. For hydrostatic tension test of PE434 foam, the hardening after yield was due to the LDPE hardening after yield.

Yield surfaces

When the deviatoric component of the initial yield stress of PS49 foam was plotted against the hydrostatic stress component (Fig. 12a), the data could be fitted quite well by an elliptical yield surface with parametric form

$$\sigma_e = 1.27 \sin\theta \quad p = 1.36 \cos\theta - 0.61 \tag{6}$$

using MPa units. The ellipse was nearly circular; its diameter along the deviatoric stress axis was 93% of the hydrostatic pressure axis diameter. Its centre was at a hydrostatic tension of 0.61 MPa. A principal-compressive-stress 'cut-off', of the type suggested [15] for PVC foam, was not needed to fit the data. Experimental data [15] for PVC closed-cell foam of density 200 kg m^{-3} was fitted with a yield surface of the same shape, but 3.3 times the size, with parametric form

$$\sigma_e = 4.2 \sin\theta \quad p = 4.5 \cos\theta - 2.0 \tag{7}$$

However, the hydrostatic tension data point [15] fell inside this ellipse. It is possible that the specimen, with six tensile 'arms' pulling on a central block, was not suitable for measuring the hydrostatic tensile yield stress; the locations of yield in the specimen were not reported.

For a particular foamed polymer, the predicted hydrostatic tension yield stress was proportional to the foam relative density R, while the numerically smaller hydrostatic compression yield stress was proportional to $R^{1.5}$. Experimental data for hydrostatic compressive yield of polypropylene foam at high strain rates, for densities between 34 and 121 kg m^{-3} [22], fit a power law relationship with exponent 1.63, with correlation coefficient $r = 0.997$. There is no experimental data to check the predicted relationship for hydrostatic tensile yield. Consequently, the shape of the yield surface will not change significantly with R, so long as $R < 0.1$. The yield surface for PS25 foam was slightly less circular than that for PS49, but the ellipse fitted the data well (Fig. 12b). The data for PE43 foam was a less good fit to an ellipse, due to yield occurring in stages in uniaxial tension—this value was ignored in determining the ellipse parameters (Table 6).

Discussion

The predicted deviatoric stress versus hydrostatic stress plots for the initial yield surfaces of three low-density polymer foams were nearly circular, in spite of the deformation mechanisms changing with the stress state. Their shapes are similar to those measured for PVC foam of density 200 kg m^{-3} [15] and EPS of density 16 kg m^{-3} [16]. This appears to be the first prediction of yield surfaces of closed-cell polymer foams, which is based on a microstructural model geometrically similar to real foams. Although the model is slightly anisotropic, this has little effect on the shape of the yield surface. When more polymer foam yield surfaces have been determined experimentally, the theory can be checked more thoroughly. The model suggests that it was incorrect to assume [20] that $p_t = p_{C0}$ (a yield surface ellipse centred at zero hydrostatic tension, Fig. 1) for extruded (anisotropic) PS foam of density 35 kg m^{-3}. The model predicted that centre of the ellipse for PS49 foam was at hydrostatic tension of 0.61 MPa. The suggestion in the ABAQUS manual that p_t is between 5 and 10% of p_{C0} is probably a relic from yield surfaces for soils; it is inappropriate for polymer foams.

A near-circular initial yield surface shape was used in the *crushable foam* material model in ABAQUS. In simulations of the indentation of a block of PS35 foam by the curved side of a rigid cylinder of small radius, and the axial compression of a truncated pyramid by a flat striker, the force versus deflection predictions were within a few per cent of those made using the yield surface of Fig. 1 [20]. This is not surprising, as the average stress state in these cases is close to uniaxial compression. However, the predicted shapes of the plastic zones differed somewhat from those using the old yield surface. In future, the FEA of foam products, the near-circular yield surface shape predicted by the Kelvin model should be used.

The model predicted that, when the applied stress(es) is(are) compressive, elastic buckling of cell faces causes stress–strain nonlinearity prior to yield. Such nonlinearity has been observed in PS foams in both uniaxial and hydrostatic compression. Unlike in solid metals, this nonlinearity does not necessarily indicate the onset of local yielding. However, elastic buckling did not cause the dry Kelvin model of LDPE foams to collapse in uniaxial compression, i.e. to undergo a high compressive strain while the stress remained nearly constant; collapse required a continuous plastic zone to spread across the model. The result expressed by Eq. 5 for bulk modulus probably applies to more than the single relative density considered here.

The Kelvin foam model predicted at least four different deformation mechanisms for yielding as the applied stress state changed (Figs. 4, 5, 6, 7, 8, 9, 10). Concertinaing of faces, after parallel plastic hinges formed across faces, was only important in uniaxial and biaxial compression. The predicted failure by face necking in tensile stress states is consistent with observations on EPS foams: in regions where a tensile failure surface transverses the beads, the faces remain flat at the failure surface. Localised thinning would not be expected in a material that was already biaxially stretched. It is hoped that future 'forensic' examination of foams, after, for example, hydrostatic compression, will reveal if the predicted mechanisms occur.

The model predicted that PS foams harden in pure shear deformation, which is known to occur experimentally [20]. Post-yield hardening was predicted to occur in compressive stress states, but not in tensile stress states. It changed with increasing strain, for a particular stress state, if further deformation mechanisms developed. Consequently, the ABAQUS crushable foam model with 'pressure-related hardening' does not realistically simulate the hardening of low-density polymer foams. The assumption of this model, that the hydrostatic tension yield stress is independent of the plastic strain, is confirmed here for PS foams (biaxially drawn polystyrene is perfectly plastic after tensile yield) but not for LDPE foams.

The EPS foams have both bead- and cell-level microstructures. When EPS foams fracture under a tensile stress, the fracture surface often follows bead boundaries, due to the lower tensile strength prevailing there. The yield surface would need adaptation to incorporate such behaviour, by including a principal-tensile-stress cut-off.

Conclusions

The deformation mechanisms in closed-cell polymer foams were predicted to be a function of the stress state. Although face concertinaing was dominant in uniaxial and biaxial compressions, it did not occur in other stress states. For stress states that involve one or more tensile principal stresses, foam yield involves in-plane extension of cell faces—hence, post-yield hardening of the foam depends on the polymer response; polystyrene foams are predicted to harden less than polyethylene foams.

The yield surface of low-density closed-cell polymer foams was predicted to be nearly circular, when plotted as deviatoric stress versus hydrostatic stress. This is consistent with the limited available experimental data.

Acknowledgement The author wishes to thank the University of Birmingham computer centre for allowing the use of the IBM Blue Bear cluster to facilitate this study.

References

1. Mills NJ (2007) Polymer foams handbook—engineering and biomechanics applications and design guide. Butterworth Heinemann, Oxford
2. Viot P, Plougonven E, Bernard D (2008) Compos Part A 39:1266
3. Mills NJ, Gilchrist A (2007) J Mater Sci 42:3177. doi:10.1007/s10853-006-1357-0s
4. Kraynik AD, Reinelt DA, van Swol F (2003) Phys Rev E67:031403
5. Kraynik AD, Warren WE (1994) In: Hilyard NC, Cunningham A (eds) Chapter 7 in Low density cellular plastics. Chapman and Hall, London
6. Weaire D, Phelan R (1994) Phil Mag Lett 69:107
7. Thomson W (1887) Phil Mag 24:503, reproduced in The Kelvin problem, D Weaire (ed), Taylor and Francis, 1996
8. Kraynik AM, Neilsen MK, Reinelt DA, Warren WE (1999) In: Sadoc J, Rivier N (eds) Foams and emulsions. Kluwer, Dordrecht, p 259
9. Mills NJ, Stämpfli R, Marone F, Brühwiler P (2009) Int J Solids Struct 46:677
10. Mills NJ (2010) Int J Solids Struct, submitted
11. Di Landro LL, Sala G, Olivieri D (2002) Poly Test 21:217
12. Gibson LJ, Ashby MF, Zhang J et al (1989) Int J Mech Sci 31:635
13. Daxner T, Bitsche RD, Böhm HJ (2006) Mater Trans 47:2213
14. Hanssen AG, Hopperstad OS, Langseth M et al (2003) Int J Mech Sci 44:359
15. Deshpande VS, Fleck N (2001) Acta Mater 49:1859
16. Leo CJ, Kumruzzaman M, Wong H, Ying JH (2008) Geotext Geomembr 26:175
17. Mills NJ, Gilchrist A (2008) Int J Impact Eng 35:1087
18. Mills NJ, Wilkes S, Derler S, Flisch A (2009) Int J Impact Eng 36:913
19. ABAQUS 6.8 (2008) Hibbert, Karlson and Sorenson, Inc., Pawtucket, RI
20. Gilchrist A, Mills NJ (2001) Int J Impact Eng 25:767
21. Surface Evolver (2004) at www.susqu.edu/facstaff/b/brakke/evolver/
22. Viot P (2009) Int J Impact Eng 36:975